



Article

High Performance Fine-Grained Biodegradable Mg-Zn-Ca Alloys Processed by Severe Plastic Deformation

Alexei Vinogradov ^{1,2,*} , Evgeni Vasilev ², Vladimir I. Kopylov ³, Mikhail Linderov ² , Alexander Brilevesky ² and Dmitry Merson ²

¹ Department of Mechanical and Industrial Engineering, Norwegian University of Science and Technology–NTNU, Trondheim N-7491, Norway

² Institute of Advanced Technologies, Togliatti State University, 445020 Togliatti, Russia; evg.vasilyev11@gmail.com (E.V.); dartvi@gmail.com (M.L.); alexandrbril@yandex.ru (A.B.); d.merson@tltsu.ru (D.M.)

³ Lobachevsky State University of Nizhni Novgorod, 603950 Nizhnij Novgorod, Russia; kopylov.ecap@gmail.com

* Correspondence: alexei.vinogradov@ntnu.no, Tel.: +47-7-359-3769

Received: 29 November 2018; Accepted: 1 February 2019; Published: 5 February 2019



Abstract: The tensile strength, fatigue, and corrosion fatigue performance of the magnesium alloy ZX40 benefit strongly from hybrid deformation processing involving warm equal-channel angular pressing (ECAP) at the first step and room temperature rotary swaging at the second. The general corrosion resistance improved as well, though to a lesser extent. The observed strengthening is associated with a combined effect of substantial microstructure refinement down to the nanoscale, reducing deformation twinning activity, dislocation accumulation, and texture transformation. The ultimate tensile strength and the endurance limit in the ultrafine-grained material reached or exceeded 380 and 120 MPa, respectively, which are remarkable values for this nominally low strength alloy.

Keywords: magnesium alloys; processing; microstructure; mechanical properties; fatigue

1. Introduction

In recent years, there has been a surge of interest in magnesium and its alloys as revolutionary materials for biomedical applications. Many modern magnesium alloys are considered as the new generation of temporal implant materials for bone fixtures, total joint arthroplasties, cardiovascular stents, wire, etc., due to their excellent functional efficiency manifested in the outstanding specific strength and very good biocompatibility and biodegradability [1–4]. In the search for efficient biodegradable materials, much attention has been paid to binary Mg-Zn, Mg-Ca, and ternary Mg-Zn-Ca and Mg-Zn-Y (or Mg-Y-Zn) biocompatible systems [5–10]. One of the key issues associated with Mg-alloys is their poor chemical stability and too high corrosion rates. Using the guiding principles based on a combination of very high purity with a thermodynamic design of the alloy microstructure, Hofstetter et al. [11–13] have demonstrated a remarkably good combination of mechanical and corrosion properties in Mg-Zn-Ca alloys ZX10 and ZX50, containing a specific noble intermetallic $Mg_6Zn_3Ca_2$ phase.

Among other issues, including biocompatibility, non-toxicity, controlled bio-degradability, etc., the use of materials as temporary implants stipulates stringent requirements on long-term mechanical properties, which are necessary to hold the integrity of implanted constructions over the whole period of healing. Apparently, fatigue and corrosion fatigue properties are of principal concern to this end.

In the present paper, we endeavour to demonstrate that employing a hybrid two-step processing scheme involving warm equal-channel angular pressing (ECAP) followed by cold rotary swaging of ZX40 Mg-Zn-Ca alloy yields an outstanding combination of a very high strength (in excess of 380 MPa) and excellent fatigue resistance (over 110 MPa in symmetrical cyclic loading) at room temperature.

For structural materials, a traditional high cycle fatigue improvement strategy relies on the empiric correlation between the monotonic strength and fatigue life, which is implicit in the well-known Basquin law, and which explains that the higher the strength under monotonic loading, the higher is the endurance limit [14]. This relation generally holds true for commercial Mg-based alloys [15]. Even though this is not a “firm” law, the increasing monotonic strength is often considered as a necessary prerequisite for improving the high cyclic fatigue performance. Severe plastic deformation (SPD) resulting in remarkable microstructure refinement and effective texture modification concomitantly with strength enhancement appears as an ideal tool for the successful implementation of this strategy for Mg alloys. A broad variety of SPD techniques have been proposed for materials processing, microstructure refinement, and strengthening [16–19]. None of those can be considered universal. Rather, they have been developed for different purposes, and therefore their joint applications can yield a synergistic effect for achieving a beneficial combination of properties. By integrating warm ECAP and cold working, the residual ductility after ECAP can be ‘converted’ into strength via further grain refinement and/or dislocation hardening, as has been successfully demonstrated for Ti [20]. Particularly, for deformation processing of rods, rotary swaging (RS) is a well-established and promising deformation technique, which belongs to a family of radial hammer forging processes for axisymmetric rods [21–23]. The mechanics of the materials plastic flow during RS has been well understood and described [21]. In multiple-step swaging processing of metallic rods, the reduction of the cross-section can be significant. Therefore, similarly to the vast majority of deformation processes, rotary swaging is accompanied by grain refinement, which in turn results in the corresponding enhancement of mechanical properties, depending on processing parameters such as temperature and extrusion ratio. While Wang et al. [23] and Alkhazraji et al. [24] have successfully applied RS to fabricate high strength Ti rods, Müller et al. [25], Gan et al. [26,27], and Minarik et al. [28] have convincingly demonstrated the viability of warm RS for deformation processing of commercial as-cast pure Mg, AZ31, and AE42 magnesium alloys.

2. Materials and Methods

Ingots of commercial purity ZX40 series Mg-Zn-Ca gravity cast alloys with the nominal composition Mg-4Zn-0.1Ca and Mg-4Zn-0.56Ca were homogenized at 350 °C for 24 h. Then the pre-heated billets were subjected to two isothermal ECAP passes through the 90° rectangular die with sharp corners. ECAP was performed at 350 °C with the ram velocity of 0.4 mm/s and the equivalent strain imposed per pass 1.15. The working billet was rotated by 90° between passes (Route B_C). Part of the ECAP processed billets of the alloy with 0.1 wt% Ca of 14×14 mm² cross-section was machined to cylindrical rods of 14.3 mm diameter which were then two-pass rotary swaged with the extrusion ratio 1.55 at room temperature. The total equivalent accumulated strain was of 2.74. Mg-alloys are hard to deform even under high hydrostatic pressure [29]. Not only the insufficient number of slip systems contribute to this difficulty, but so does the excess fraction of intermetallic phases. Therefore, the RS processing was limited to the alloy with the low Ca content (0.1 wt.%), while the alloy ZX40-0.56Ca was left in the ECAP state for comparison.

The specimens for metallographic observations were ground and mechanically polished down to 0.25 µm and then etched in a solution containing 50 ml distilled water, 150 ml ethanol, and 1 ml acetic acid. Microstructural observations were carried out using an inverted optical microscope Zeiss Axiovert (Ulm, Germany) with the image analyzing metallographic software Thixomet™ (Thixomet, St. Petersburg, Russia) and a field emission gun scanning electron microscope (SEM) Zeiss SIGMA (Jena, Germany) equipped with the Hikari electron backscattering diffraction (EBSD), (EDAX/TSL, Mahwah, NJ, USA) camera and orientation image microscopy (OIM-6.2, EDAX/TSL,

Mahwah, NJ, USA) software package. Prior to EBSD microstructural investigations and mechanical testing, the samples were gently mechanically polished to a mirror-like finish and then electrolytically polished in 90% ethanol + 10% nitric acid solution. The further detailed microscopic observations were conducted using the Philips CM12 transmission electron microscope (TEM) at an accelerating voltage of 200 kV. Specimens for TEM observation of the SPD-produced microstructure were taken from the middle part of the billet perpendicular to the extrusion direction (ED) and parallel to it (in the TD direction). Thin foils were prepared using ion milling. Observations were carried out in both a bright and dark field. Phase identification was carried out by X-ray diffraction (XRD), using an XRD-7000 (Shimadzu, Kyoto, Japan) $\theta-2\theta$ diffractometer (Cu K α radiation) in the 10–90° 2θ range with 0.015° scan steps.

The specimens for mechanical testing were cut using spark erosion from the central part of the ECAP-ed or RS-processed billets in the longitudinal direction, i.e., along the extrusion direction. Uniaxial tensile tests were conducted on conventional I-shaped specimens with the $10 \times 4 \times 3 \text{ mm}^2$ using the screw-driven testing machine (Kammrath & Weiss, Germany) under constant crosshead velocity corresponding to a nominal strain rate of $1 \times 10^{-4} \text{ s}^{-1}$ (per ASTM E8 recommendations). An axial extensometer was used to measure the strain during tension, and each test was repeated for at least three samples. For fatigue testing, the sub-size hourglass specimens with the minimum cross-section of $2 \times 2 \text{ mm}^2$ were used. The shapes and dimension of the specimens used for mechanical testing are shown in the corresponding figures in the following sections. The small size of the specimens is dictated by the final diameter of the rod and is typical for the SPD-manufactured materials. As has been shown [30], the rescaling of the ECAP-ed ZX60 specimen size does not affect the results of fatigue tests appreciably. An Instron Electropuls E1000 (Instron, High Wycombe, UK) electro-mechanical testing machine operating in the symmetric push-pull cycling ($R = -1$) mode was used for cyclic testing (per ASTM E466 recommendations) at ambient temperature in dry air and in corrosive media at constant stress amplitude $\Delta\sigma/2$ at 100 Hz frequency.

Various methods, which have been devised to characterize corrosion properties and to elucidate the underlying corrosion mechanism, include a family of potentiostatic and dynamic electrochemical methods, impedance spectroscopy, hydrogen evolution, etc. [31,32]. Among those, the simplest weight-loss method [33] is still used as a “golden standard” direct corrosion test even though it does not render any information about the corrosion mechanism. Ideally, the measurement of the hydrogen evolved is equivalent to the measurement of the weight loss of the metal [34], provided the uncertainties associated with both methods are alleviated. The plate specimens with the surface area of 650–800 mm² were ground by sandpaper down to #2500 grade, washed in the ultrasonic bath with acetone, dried and weighed on the analytical balance with the accuracy of 0.0001 g. They were then immersed into 0.9% NaCl distilled water solution ($\text{pH} = 7.4 \pm 0.2$) for 24 h at 25 °C. The corrosion products were carefully removed from the surface by the solution containing 200 g of CrO₃, 10 g of AgNO₃ and 1000 cm³ of distilled water at 20–25 °C. The specimens were then immediately dried and weighed again. All test repeated at least three times.

For corrosion fatigue testing aiming at the approximate assessment of the corrosion fatigue performance of the alloys studied, a home-designed thermally-stabilized acrylic chamber was assembled on the testing machine so that the gage length of the sample was permanently immersed in the circulating 0.9% NaCl solution at 37 ± 1 °C. The testing cell was connected with the bath containing 10 l of the corrosive solution which was pumped through the cell at a rate of 0.5 l/min. The large volume of the testing solution, small specimen size, and relatively short testing time, which did not exceed 24 h, ensured the relatively stable pH value throughout the test as it is recommended in the ASTM NACE/ASTM G31-12a standard.

Ending this section, we have to briefly explain the choice of the corrosive media for this study. Currently, many different pseudo-physiological solutions are used for in vitro testing of materials aimed at biomedical applications. Besides the NaCl saline solution, these include, although not limited to, Hank’s solution, a family of modified SBFs, Ringer’s solution, Tas-SBF, etc., differed by main ion

concentrations to mimic the compositions of human blood plasma [35–37]. The crucial question is which one to be chosen to assess the corrosion/corrosion fatigue properties in vitro, on one hand, and to get the results which can be translated to the in-vivo tests, on the other? The only existing consensus in the abundant literature is that none of the existing solutions can really replicate the conditions in the human body to the desired extent, even though the judicious choice of the testing SBF can significantly reduce the number of specimens needed for testing in vivo [35,36]. Furthermore, they all cause different electrochemical responses from the materials tested, and, more importantly for the present preliminary study, they result in the significantly more complicated surface layer containing, besides magnesium hydroxide, complex oxides including P, Ca, O, and Mg [38]. Since the surface conditions strongly affect the fatigue/corrosion fatigue behavior, which has been poorly understood so far, the additional complication in the form of the extra surface layer can be alleviated by using a simple NaCl solution, which is also most widely used for characterization of corrosion fatigue in structural Mg alloys.

3. Results and Discussion

3.1. Microstructure

The typical microstructure of the as-cast Mg-Zn-0.1Ca alloy after homogenization annealing is shown in Figure 1a. The similar grain structure is frequently observed in Mg-Zn-Ca alloys [39–41]. Precipitates form in Mg-Ca alloy even at low Ca addition or rapid solidification because of the very low solubility of Ca in Mg at room temperature [42]. Similarly to the results reported in the abundant literature (see, e.g., References [41,43]), the homogenized ZX40 Mg-4Zn-0.1Ca alloy consists of almost equiaxed grains with the average grain size of 220 μm , while intermetallic particles preferably in the round shape are distributed around grain boundaries or in grain interior. These particles are commonly identified as the $\text{Ca}_2\text{Mg}_6\text{Zn}_3$ phase [6–8,44] in good agreement with thermodynamic predictions [45,46]. The Mg_2Ca phase, which is often observed in Mg-Ca and some Mg-Zn-Ca alloys [47,48], is not found in the present as-cast alloy. It has been reported that the formation of Mg_2Ca in Mg-Zn-Ca alloys depends on the Zn/Ca atomic ratio: when this ratio is greater than 1.23, the Mg_2Ca phase does not form [49]. The results of the SRD scans shown in Figure 2 fully corroborate these findings. Distinct peaks associated with α -Mg and the ternary $\text{Ca}_2\text{Mg}_6\text{Zn}_3$ compound are observed, whereas there is no information regarding the binary Mg_2Ca phase available. The increasing concentration of Ca to 0.56 wt.% results reasonably in the increased volume fraction of the second phase but does not change the phase composition, as seen in Figure 2.

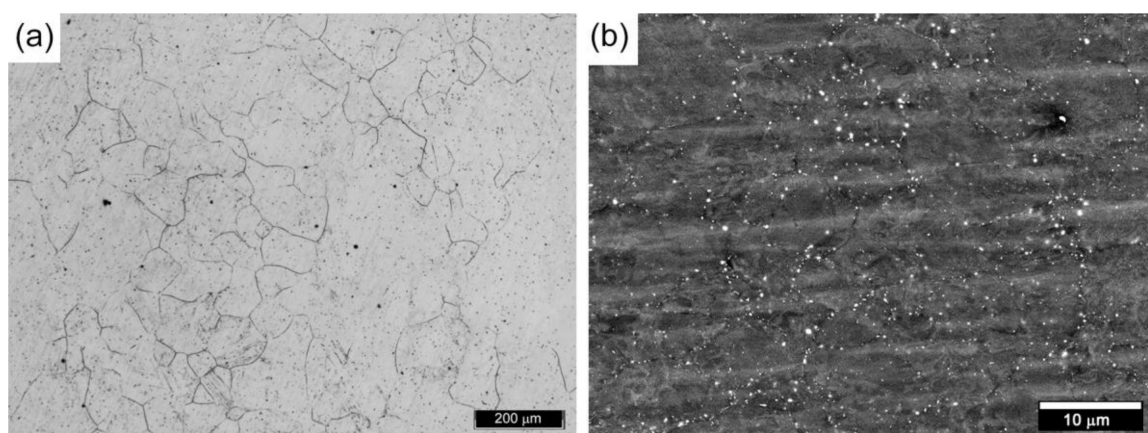


Figure 1. The microstructure of the ZX40 alloy (0.1 Ca) specimens showing the distribution of second phases. (a) Optical microscopy image of the as-homogenized specimen; (b) SEM image in the back-scattered electron contrast of the specimen after equal-channel angular pressing (ECAP).

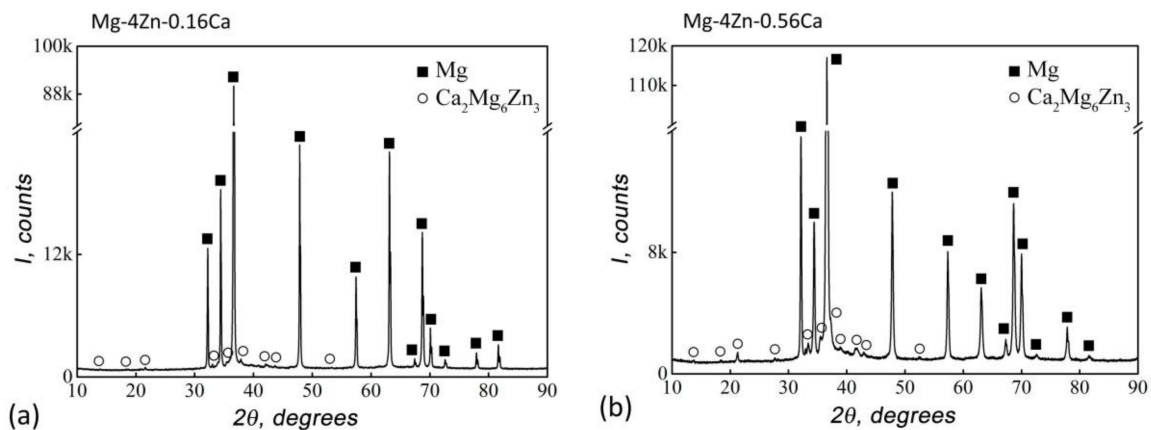


Figure 2. The X-ray diffraction pattern of the as-cast ZX40 Mg-Zn-Ca alloys with different content of Ca (a) Mg-4Zn-0.16Ca, (b) Mg-4Zn-0.56Ca.

Figure 3 shows the grain orientation maps of the alloy ZX40-0.1Ca cross-section normal to the extrusion direction (ED) after ECAP and ECAP+RS processes. The observed grain microstructure across the processed billets was nearly uniform, except the region close to the edge of the ECAPed and RS-processed samples. It is worth noticing that the recent investigation by Charni et al. [50] has demonstrated that the RS strongly influences the properties and the fluctuation of the residual stresses near the surface, while a few hundred micrometers below the surface, the workpiece properties are driven only by the total deformation. Thus, due to the proper shaping of the specimens, the possible effects of residual stresses are alleviated in the present work. The corresponding grain size distributions (with edge grains excluded) and the distribution of the angles of misorientation between neighboring grains are shown in Figure 4 for both ECAPed and post-ECAP rotary swaged samples. As can be seen from both figures, ECAP resulted in considerable refinement of the as-cast grains reduced from 220 μm to about 20–30 μm . Concurrently, some modest refinement and redistribution of the second phase are observed in Figure 1b. The microstructure after ECAP consisted predominantly of nearly uniform, fine, equiaxed, and recrystallized grains. Although these grains represent the main units in the microstructure, some initial, coarse, un-recrystallized grains are also seen here and there on the EBSD maps obtained within the working billet. Overall, the grain size distribution after ECAP is admittedly wide, being indicative of a microstructure, containing a mixture of large and small grains with the weighted mean of 27.5 μm , and the standard deviation of 12.6 μm . Thus, the microstructure of the ECAPed to 2 passes of the ZX40 alloy can be regarded as heterogeneous, as it is commonly observed in this class of alloys. The benefits of the strongly heterogeneous (e.g., bi-modal) microstructure are also commonly associated with the outstanding combination of good strength provided by the fine grain structural component and ductility due to the greater deformation capacity of coarse grains [51–53].

Further significant grain refinements were observed after rotary swaging. The grain size distribution becomes narrower than that in the ECAPed specimen, and the sample weighted mean and the standard deviation are reduced to 10 μm and 5.5 μm , respectively. However, the heterogeneity of the microstructure remained or even increased due to the very fine sub-microcrystalline grains coexisting with the original coarse grains. Importantly, as can be seen from Figure 4, not only the grain size was refined substantially during post-ECAP rotary swaging, but also the preferred crystallographic grain orientation changed remarkably, as will be discussed in further details below.

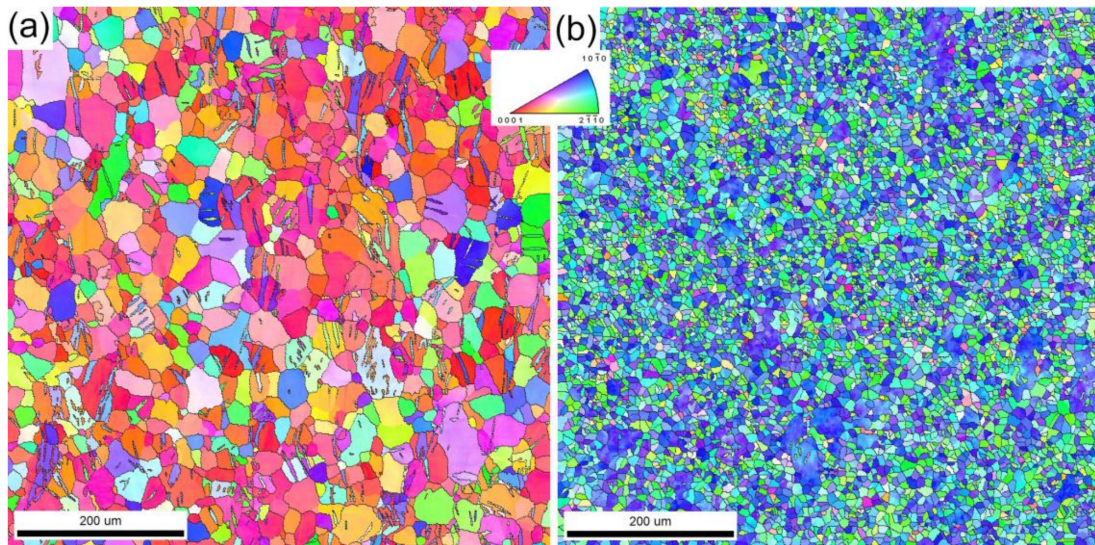


Figure 3. Inverse pole figure colored electron backscattering diffraction (EBSD) orientation maps of the alloy ZX40 cross-section normal to the extrusion direction; after (a) ECAP and (b) ECAP+RW processes. The color code is shown in the inset as a standard stereographic triangle for both maps.

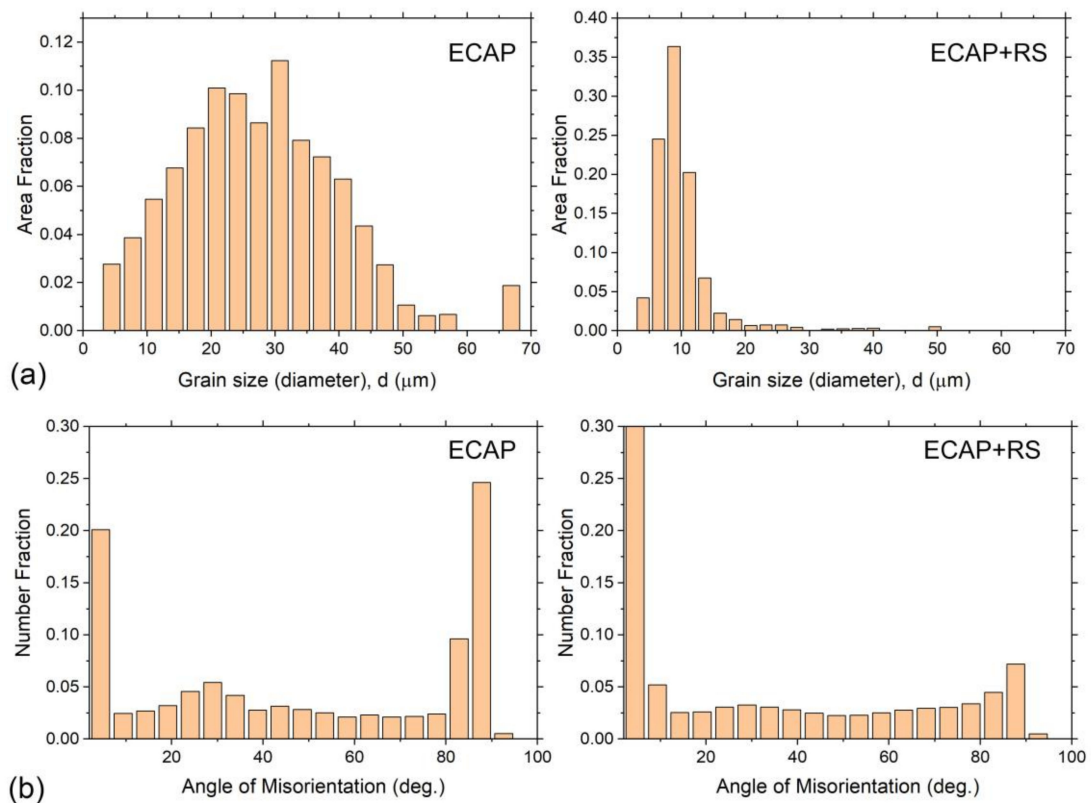


Figure 4. Distributions of grain sizes (a) and misorientation angles (correlated) between neighboring grains (b) in the ZX40 Mg alloy after hot ECAP and ECAP followed by cold rotary swaging processing (marked on corresponding sub-figures).

A large number of mechanically twinned regions is evident from the IPF map of the ECAPed specimen, Figure 3a, showing that large plastic strains imposed during ECAP cannot be completely accommodated by basal and pyramidal slip events at such a high deformation temperature as 350 °C. The same is seen on the misorientation angle distribution of boundaries (including low angle boundaries, high angle boundaries, and twin boundaries), Figure 4b. The distribution of the

misorientation angles exhibits two pronounced maxima in the high angle domains, one between 30 and 40°, and the other one at around 85–90°. A misorientation angle of 86.4° corresponds to the lattice rotations due to $\{10\bar{1}2\}\langle 10\bar{1}1\rangle$ extension twins. The double-twinning, which often occurs in magnesium alloys and which results in characteristic angular misorientations of 38° in the respective histograms [54], is not very pronounced, as seen in Figure 4b.

The relative fraction of extension twins was reduced after rotary swaging. However, this might be observed due to a significant increase in the presence of small angle misorientations, as can be seen in Figure 4b. The large fraction of low angle boundaries in both (ECAP and ECAP+RS) specimens is indicative of significant strain hardening due to dislocation accumulation in sub-grain boundaries during deformation, which is particularly noteworthy at low deformation temperatures.

3.2. Mechanical Properties

Figure 5 shows the tensile stress-strain diagrams for the ECAP and ECAP+RS processed samples. A trade-off between tensile strength and uniform elongation is seen as it is commonly reported for the vast majority of SPD manufactured metals and alloys [16,55,56]. Cold deformation reduces the average grain size, and the tensile strength increases spectacularly to the very high value of 380 MPa (unprecedented for this class of low strength alloys). Concurrently, the elongation to failure reduces, albeit not to a prohibitively low level, depending on application needs.

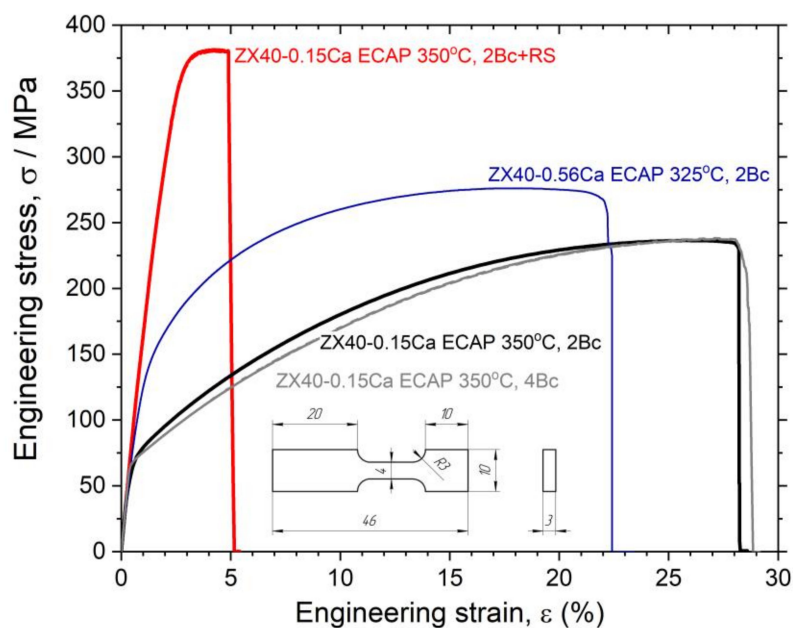


Figure 5. The tensile stress-curves of ECAPed and ECAP+RS processed ZX40 alloys. The specimen shape and dimensions are shown in the inset.

The fatigue S-N curves for the alloys ZX40 are displayed in Figure 6 together with reference data for the hot extruded alloys WE43 (RE-alloyed) [57] and ZX20 (same Mg-Zn-Ca system as in the present study) [58], and the popular fine-grain ZK60 Mg-6.0Zn-0.5Zr alloy manufactured by multiaxial isothermal forging (MIF) [30]—all tested in air—(see References [59,60] for processing details).

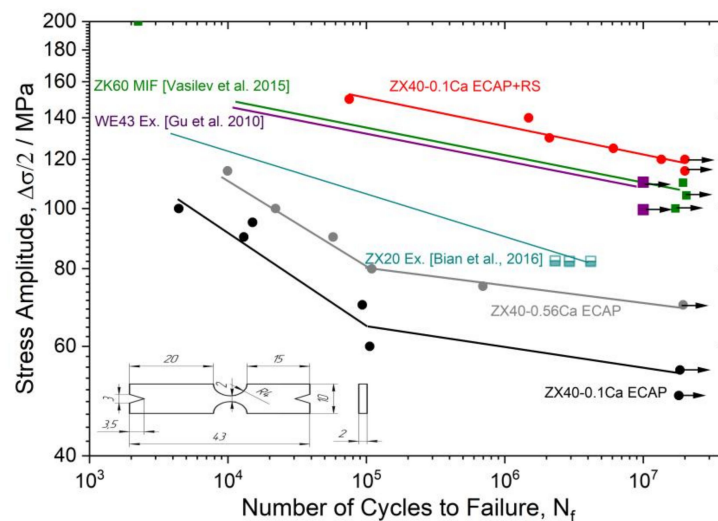


Figure 6. Wöhler S-N diagrams for ECAPed and ECAP+RS processed ZX40 alloys tested in dry air. The specimen shapes and dimensions are shown in the inset. Literature data for the reference ZX20, WE43, and ZK60 alloys (also tested in air) are shown for comparison.

While the ECAPed material demonstrates only modest fatigue properties typical of many wrought Mg-based alloys [61], the fatigue endurance of the rotary swaged samples is remarkably improved to up to 125 MPa at 10^7 cycles, which is more than doubled compared to its ECAPed counterpart having $\sigma_{-1}=55$ MPa. It is also notably higher than σ_{-1} values reported for the fine-grained high strength MIF-processed ZK60 alloy, and conventionally extruded advanced WE43 and ZX20 biodegradable alloys, which are considered for biomedical applications. The favorable comparison with the alloys ZK60 and WE43 is particularly noteworthy since both these alloys have been recognized for their excellent mechanical properties. Furthermore, WE43 has already been deployed in biomedical (stent) applications and is therefore often used a reference for chemical and mechanical performance [62,63]. Relatively strongly alloyed by Rear Earth elements, (3.7–4.3Y, 2.4–4.4 RE (Nd and Yb, Er, Dy, Gd)) this alloy is nominally positioned as a high strength alloy. Thus, we believe that the obtained combination of excellent tensile and fatigue strengths in the alloy ZX40 is promising for a wide range of applications of these lightweight biocompatible and biodegradable alloys.

Considering the sub-size geometries of the specimens (shown in the inset in Figure 6) used to evaluate the high cycle fatigue performance, estimating the theoretical elastic stress concentration factor k_t for a given curvature of the hourglass shaped specimen as 1.31, and having the notch sensitivity q of typical Mg alloys of the order of 0.25–0.5 [61], one can reasonably expect the actual fatigue limit of the materials tested to be 5–10% larger than that reported in Figure 6. Mechanical properties in tensile and cyclic deformation are summarized in Table 1.

However, before any conclusion can be made with confidence on the possible benefits of biomedical and other applications of materials, the assessment of their degradation in the biological environment has to be done both *in vitro* and *in vivo*. In general, when metals are exposed to the simultaneous actions of cyclic stress and a corrosive environment, the fatigue behavior changes dramatically compared to that in the air [64], and the properties inevitably degrade. The same applies to Mg-based alloys where the problem is particularly acute since these materials are very susceptible to environmental conditions and their corrosion fatigue properties are often below expectations [65–67]. Apparently, the well-controlled bio-corrosion fatigue degradation is crucial for temporary implants and cardiovascular stents. Therefore, a brief excursion into the corrosion performance of Mg-based alloys is in place. In corrosion fatigue, the knee in the Wöhler curve usually disappears, and materials do not exhibit a fatigue limit. The fatigue limit reported by Gu et al. [57] for the conventionally extruded WE43 alloy in the air was of 110 MPa at 10^7 number of cycles. This value, however, dropped to 40 MPa at the same number of cycles in the simulated body fluid (SBF) at 37 °C. Magnesium undergoes pitting

corrosion when exposed to chloride ions in non-oxidizing solutions [68,69]. The corrosion fatigue crack initiates most naturally from a corrosion pit. Therefore, the rule of thumb is that the longer the induction time for pit formation, the greater the corrosion fatigue life. General corrosion and corrosion fatigue properties of the studied alloys ZX40 are represented in Table 1 in terms of the corrosion rate CR determined by the immersion test in the Saline solution (c.f. Reference [33] for the methodological details) and the corrosion fatigue life measured at the stress amplitude $\Delta\sigma/2 = 35$ MPa in the same solution. Obviously, fatigue life is reduced dramatically. Among the others, the fine-grained ECAP+RS specimen demonstrates the slightly smaller corrosion rate (that agrees with the frequently observed effect of the grain size on corrosion properties [70]), and somewhat better corrosion fatigue life for which the effect of grain size has not been well understood yet. The corrosion rate estimated after the 24 h immersion test is apparently higher than expected from a long-term test, e.g., 7 days longer, (per the ASTM NACE/ASTM G31-12a standard), c.f. Reference [33], and it appears to be within the reasonably estimated range for this class of alloys. We should notice that only preliminary results of corrosion fatigue testing are presented here to illustrate the trends in the environmentally assisted fatigue behavior of Mg alloys. More detailed results including corrosion fatigue testing in both NaCl solution and SBF with the corresponding analysis of the S-N curves will be reported elsewhere in a dedicated publication.

Table 1. Mechanical and corrosion properties of bio-degradable Mg-based alloys.

Alloy/Composition	Processing	d , μm	$\sigma_{0.2}$, MPa	σ_{UTS} , MPa	ε_f , (%)	σ_{-1} , MPa	N_{fc}	CR, mm/year
ZX40 A/Mg-4.0Zn-0.1Ca	ECAP, 325 °C	28 ± 13	71 ± 4	265 ± 3	20 ± 2	55 ± 3	1.0×10^5	4.4 ± 0.2
ZX40 A/Mg-4.0Zn-0.1Ca	ECAP+RS	10 ± 6	348 ± 5	381 ± 5	5.0 ± 0.5	118 ± 3	1.7×10^5	3.0 ± 0.2
ZX40 B/Mg-4.0Zn-0.56Ca	ECAP, 325 °C	9 ± 7	127 ± 3	271 ± 6	22 ± 2	70 ± 3	7.5×10^4	2.4 ± 0.5
ZX20 /Mg-2Zn-0.2Ca [50]	Hot extruded	-	118 ± 6	211 ± 11	24 ± 1	80*	-	-
ZK60 [51]	MIF** 300 °C	5 ± 4	235 ± 7	328	31 ± 3	105 ± 3	$3-7 \times 10^5$	2.6 ± 0.5

* At 4×10^6 cycles; ** MIF—multiaxial isothermal forging. d —grain size, $\sigma_{0.2}$ —conventional yield stress, σ_{UTS} —ultimate tensile strength, ε_f —elongation at break, σ_{-1} —fatigue limit at symmetrical push-pull testing (in air) at 10^7 number of cycles, N_{fc} —fatigue life at the stress amplitude $\Delta\sigma/2 = 35$ MPa (in 0.9 wt.% NaCl), CR—corrosion rate, mm/year (in 0.9 wt.% NaCl).

3.3. Texture Analysis

The mechanical behavior of magnesium alloys depends strongly on texture due to the inherent anisotropy of their hexagonal crystal lattice [71,72]. The texture development in Mg alloys has been extensively studied and well understood for different processing routes including forging, extrusion, different variants of ECAP [73–75], and swaging [25–27]. During rolling and/or extrusion, a strong texture develops with the basal plane perpendicular to the deformation direction [76–78]. This texture tends to retain after recovery and recrystallization annealing [79]. A great deal of work has been dedicated to developing a technological procedure capable of weakening the basal texture and/or reducing the critical resolved shear stresses (CRSS) of the non-basal slip systems. Among those, specific alloying, primarily with Rare Earth elements [80] (with regard to the present work, it should be noticed that the addition of calcium into the Mg-Zn system also weakens the strong basal textures and promotes grain refinement during hot-extrusion of Mg-Zn-Ca and Mg-Zn-Al-Ca alloys due to the particle stimulated nucleation of dynamic recrystallization [81,82]), and imposing shear deformation, e.g., via asymmetrical rolling [83] or ECAP [75,84–86] have gained the greatest popularity. Agnew et al. [87,88] have shown that the texture becomes stronger with the increasing number of ECAP-Bc passes. It is commonly observed that, for the route Bc, ECAP deformation involving 90° rotation of the working billet around the longitudinal axis gives rise to the basal fiber, which develops at about 45° to ED, i.e., along the simple shear direction [74,85,89]. It is therefore

reasonable that the pole figures observed in the present work for ECAPed specimens, Figure 7a, demonstrate the same features in the distribution of crystallographic poles as those in the cited papers since they are deformed in the same deformation mode.

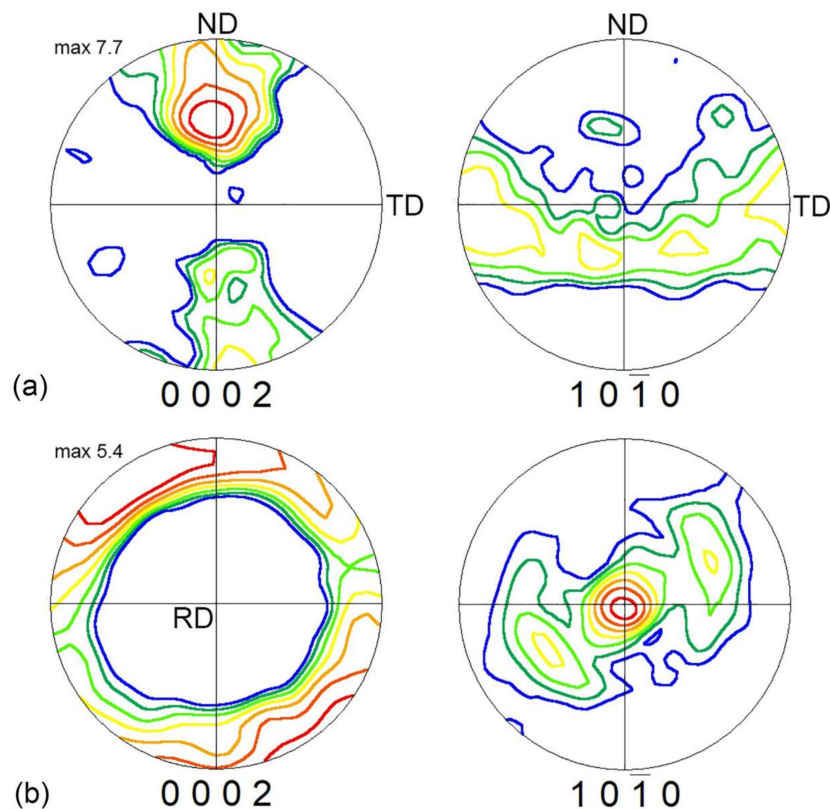


Figure 7. Pole figures obtained from EBSD data for the ZX40 Mg alloy after hot ECAP (a) and ECAP followed by cold rotary swaging processing (b).

After rotary swaging, the characteristic ECAP texture changed remarkably. This can be evidently seen from the pole figures shown in Figure 7a (also compare the IPF maps in Figure 3). A strong $\{0001\}$ basal fiber is observed, as is commonly reported for magnesium after swaging [27]. The $\{0001\}$ basal plane intensity decreased slightly compared to that after ECAP. As has been noticed by Gan et al. [27], the materials flow during swaging deformation resembles that during multiple axial forging and extrusion of a working billet, whereas the simple shear is the main deformation mode in ECAP [90]. As a result, the predominant basal slip accommodated by twinning deformation gives rise to the strong basal fiber texture, which is very similar to that reported in early publications dealing with the swaging of magnesium alloys [25–27]. The dynamic recrystallization is not expected during swaging due to a low processing temperature, while the observed increasing low angle misorientations in the distributions shown in Figure 4b strongly suggest that the strengthening observed after the hybrid ECAP+RS processing is the result of the combined effect of grain refinement and strain hardening due to the dislocation accumulation in the grains. Low swaging temperature hinders both dislocation recovery and recrystallization, promoting dislocation storage in the grains. This is also corroborated by TEM observations discussed below.

3.4. TEM Observations of the Microstructure of the Rotary Swaged Specimens

To get a better understanding of the microstructural factors promoting the greatly enhanced strength of the rotary swaged ZX40 alloy, TEM observations have been performed. The images of the grain microstructure in both longitudinal and transverse directions in Figure 8 clearly show that along with the relatively large grains (still only several micrometers in diameter and

which are nicely revealed by the EBSD analysis in Figure 3), there have been many very fine nano-size dislocation-free recrystallized grains with high-angle boundaries distinguishable within larger original grains. The selected area microdiffraction patterns demonstrate the presence of large azimuthal misorientations corresponding to a large number of very small, sub-microcrystalline grains. However, the sub-grains with low angles of misorientation are also clearly visible in the micrographs, as is also suggested from the EBSD analysis of local misorientations. The sizes of many individual grains appear to be in the range of 40–60 nm, which is admittedly very small for magnesium. The increasing fraction of grains of this size in the microstructure obviously contributes to the significant increase in the monotonic and cyclic strength shown in Figures 5 and 6.

Dislocations are distributed non-uniformly. The density of dislocations is noticeably higher in large grains. The dislocations tend to arrange themselves into walls with low-angle misorientations, which are also identified in the EBSD measurements and which give rise to the pronounced peak in the distributions of misorientation angles, Figure 4b. Although twin lamellae of a characteristic lenticular shape are observed sporadically in relatively coarse grains, it should be noticed that the number and volume fraction of the twins is relatively small.

Thus, TEM helps to reveal the fine changes that occurred in the microstructure after hybrid deformation processing through ECAP followed by cold rotary swaging. These factors include the heterogeneous dislocation density with excess dislocation populations in large grains and very low populations in small grains, suppression of mechanical twinning in fine grains, and the formation of a nano-grained structure. It is quite obvious that the key to the further control of the mechanical properties will be a change in the combination of the above factors towards the formation of an even more uniform microstructure and an even more uniform distribution of particles of hardening phases.

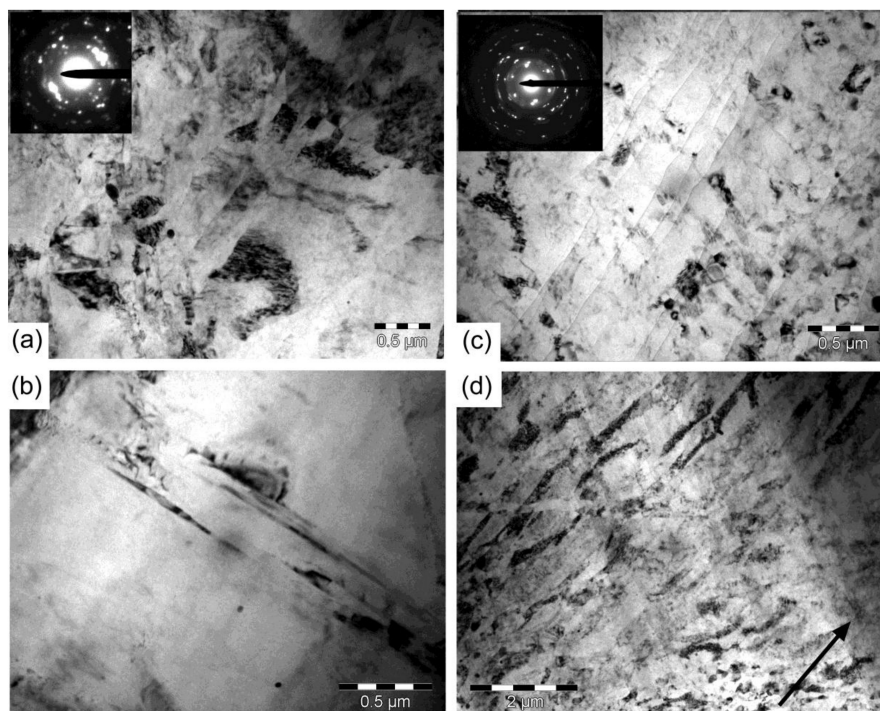


Figure 8. Bright field TEM images and corresponding selected area electron diffraction patterns representing the typical fragments of the microstructure of the ECAP+RS processed specimen; thin foils are obtained from the cross-section perpendicular to the extrusion direction (ED) (a,b); thin foils from the cross-section parallel to ED (c,d); and the arrow in (d) indicates the extrusion direction.

4. Conclusions

- (1) Hybrid SPD processing comprised of hot ECAP and cold (room temperature) rotary swaging of magnesium alloys paves a new avenue for the fabrication of nanostructured high strength alloys that benefits from a combined effect of grain refinement down to the nano-scale with dislocation strengthening and texture transformation.
- (2) The nominally low strength Mg Zn-Ca alloys with the fine grain microstructure obtained by hybrid processing demonstrated an excellent combination of tensile and fatigue strength ($\sigma_{0.2} = 380$ and $\sigma_{-1} = 120$ MPa, respectively), exceeding those known for most conventionally processed alloys aimed at biomedical applications, though the ductility has been compromised to some extent. This combination makes these alloys appealing for a wide range of applications where weight saving and/or biocompatibility and biodegradability are of concern.

As a final note, even though biodegradability is a pivotal property for temporary implants, there is still a lot to desire for a slower biodegradability rate. Reducing the materials susceptibility to general corrosion in-vitro through chemical purity and phase composition control is step one to achieving this goal [11,12,67]. Next is the improvement of the overall fatigue performance in air through microstructure optimization by control over grain size, texture, and the distribution of primary and secondary phases. This step is an essential prerequisite for enhancing the corrosion fatigue resistance, which is usually controlled by crack initiation (i.e., by high cycle fatigue properties), and not by crack propagation (i.e., by low-cycle fatigue properties).

Several important issues have not been addressed in the present work, leaving room for further research. The topics which need to be considered include the effect of hybrid processing on the distribution second phases, the mechanism of formation of nano-grains at low homologous temperatures during processing and types of dislocations involved, the effect of post-processing annealing on the deformation behavior and ductility, optimization of the processing route, and, of course, the more detailed and systematic characterization of the corrosion/corrosion fatigue properties, morphology of the corroded surface, and degradation mechanisms in simulated body fluids.

Author Contributions: Conceptualization, A.V. and D.M.; methodology and SPD processing, V.K.; microstructural investigation and mechanical testing, E.V. and A.B; fatigue testing, M.L.; writing and editing, A.V.; project administration, D.M.

Funding: This work was supported by the Ministry of Science of RF under grant-in-aid RFMEFI58317X0070.

Acknowledgments: The skillful help by Dr. Tomas Kruml from the Institute of Physics of Materials, Brno, Czech Republic in TEM observation is gratefully appreciated. The authors are indebted to professors Y. Kawamura and M. Yamasaki (Kumamoto University, Japan) for stimulating and encouraging discussions.

Conflicts of Interest: The authors declare no conflict of interest.

References

1. Witte, F. The history of biodegradable magnesium implants: A review. *Acta Biomater.* **2010**, *6*, 1680–1692. [[CrossRef](#)] [[PubMed](#)]
2. Erinc, M.; Sillekens, W.H.; Mannens, R.G.T.M.; Werkhoven, R.J. *Applicability of Existing Magnesium Alloys as Biomedical Implant Materials*; Data Archiving and Networked Services: Amsterdam, The Netherlands, 2009; pp. 209–214.
3. Chen, Q.; Thouas, G.A. Metallic implant biomaterials. *Mater. Sci. Eng. R Rep.* **2015**, *87*, 1–57. [[CrossRef](#)]
4. Farraro, K.F.; Kim, K.E.; Woo, S.L.Y.; Flowers, J.R.; McCullough, M.B. Revolutionizing orthopaedic biomaterials: The potential of biodegradable and bioresorbable magnesium-based materials for functional tissue engineering. *J. Biomech.* **2014**, *47*, 1979–1986. [[CrossRef](#)] [[PubMed](#)]
5. Zhang, B.P.; Wang, Y.; Geng, L. Research on mg-zn-ca alloy as degradable biomaterial, biomaterials—Physics and chemistry. In *Biomaterials*; Pignatello, R., Ed.; InTech.: London, UK, 2011.
6. Lu, Y.; Bradshaw, A.R.; Chiu, Y.L.; Jones, I.P. Effects of secondary phase and grain size on the corrosion of biodegradable mg-zn-ca alloys. *Mater. Sci. Eng. C* **2015**, *48*, 480–486. [[CrossRef](#)] [[PubMed](#)]

7. Hänzi, A.C.; Gerber, I.; Schinhammer, M.; Löffler, J.F.; Uggowitzer, P.J. On the in vitro and in vivo degradation performance and biological response of new biodegradable Mg–Y–Zn alloys. *Acta Biomater.* **2010**, *6*, 1824–1833. [[CrossRef](#)] [[PubMed](#)]
8. Hänzi, A.C.; Sologubenko, A.S.; Uggowitzer, P.J. Design strategy for new biodegradable Mg–Y–Zn alloys for medical applications. *Int. J. Mater. Res.* **2009**, *100*, 1127–1136. [[CrossRef](#)]
9. Abe, E.; Kawamura, Y.; Hayashi, K.; Inoue, A. Long-period ordered structure in a high-strength nanocrystalline Mg-1 at% Zn-2 at% Y alloy studied by atomic-resolution z-contrast stem. *Acta Mater.* **2002**, *50*, 3845–3857. [[CrossRef](#)]
10. Kawamura, Y.; Yamasaki, M. Formation and mechanical properties of Mg₉₇Zn₁Re₂ alloys with long-period stacking ordered structure. *Mater. Trans.* **2007**, *48*, 2986–2992. [[CrossRef](#)]
11. Hofstetter, J.; Becker, M.; Martinelli, E.; Weinberg, A.M.; Mingler, B.; Kilian, H.; Pogatscher, S.; Uggowitzer, P.J.; Löffler, J.F. High-strength low-alloy (HSLA) Mg–Zn–Ca alloys with excellent biodegradation performance. *JOM* **2014**, *66*, 566–572. [[CrossRef](#)]
12. Hofstetter, J.; Martinelli, E.; Pogatscher, S.; Schmutz, P.; Povoden-Karadeniz, E.; Weinberg, A.M.; Uggowitzer, P.J.; Löffler, J.F. Influence of trace impurities on the in vitro and in vivo degradation of biodegradable Mg-5Zn-0.3Ca alloys. *Acta Biomater.* **2015**, *23*, 347–353. [[CrossRef](#)]
13. Hofstetter, J.; Rüedi, S.; Baumgartner, I.; Kilian, H.; Mingler, B.; Povoden-Karadeniz, E.; Pogatscher, S.; Uggowitzer, P.J.; Löffler, J.F. Processing and microstructure–property relations of high-strength low-alloy (HSLA) Mg–Zn–Ca alloys. *Acta Mater.* **2015**, *98*, 423–432. [[CrossRef](#)]
14. Roessle, M.L.; Fatemi, A. Strain-controlled fatigue properties of steels and some simple approximations. *Int. J. Fatigue* **2000**, *22*, 495–511. [[CrossRef](#)]
15. Heywood, R.B. *Designing against Fatigue of Metals*; Reinhold: New York, NY, USA, 1962; p. 436.
16. Estrin, Y.; Vinogradov, A. Extreme grain refinement by severe plastic deformation: A wealth of challenging science. *Acta Mater.* **2013**, *61*, 782–817. [[CrossRef](#)]
17. Langdon, T.G. Twenty-five years of ultrafine-grained materials: Achieving exceptional properties through grain refinement. *Acta Mater.* **2013**, *61*, 7035–7059. [[CrossRef](#)]
18. Segal, V.M. Equal channel angular extrusion: From macromechanics to structure formation. *Mater. Sci. Eng. A* **1999**, *271*, 322–333. [[CrossRef](#)]
19. Segal, V. Review: Modes and processes of severe plastic deformation (SPD). *Materials* **2018**, *11*, 1175. [[CrossRef](#)] [[PubMed](#)]
20. Semenova, I.P.; Salimgareeva, G.K.; Latysh, V.V.; Valiev, R.Z. Enhanced fatigue properties of ultrafine-grained titanium rods produced using severe plastic deformation. *Solid State Phenom.* **2008**, *140*, 167–172. [[CrossRef](#)]
21. Kegg, R.L. Mechanics of the rotary swaging process. *J. Eng. Ind.* **1964**, *86*, 317–324. [[CrossRef](#)]
22. Abdulstaar, M.A.; El-Danaf, E.A.; Waluyo, N.S.; Wagner, L. Severe plastic deformation of commercial purity aluminum by rotary swaging: Microstructure evolution and mechanical properties. *Mater. Sci. Eng. A* **2013**, *565*, 351–358. [[CrossRef](#)]
23. Wang, M.; Wang, Y.; Huang, A.; Gao, L.; Li, Y.; Huang, C. Promising tensile and fatigue properties of commercially pure titanium processed by rotary swaging and annealing treatment. *Materials* **2018**, *11*, 2261. [[CrossRef](#)]
24. ALkhazraji, H.; El-Danaf, E.; Wollmann, M.; Wagner, L. Enhanced fatigue strength of commercially pure Ti processed by rotary swaging. *Adv. Mater. Sci. Eng.* **2015**, *2015*, 12. [[CrossRef](#)]
25. Muller, J.; Janecek, M.; Wagner, L. Influence of post-ecap TMT on mechanical properties of the wrought magnesium alloy AZ80. *Mater. Sci. Forum* **2008**, *584*, 858–863. [[CrossRef](#)]
26. Gan, W.M.; Huang, Y.D.; Wang, R.; Zhong, Z.Y.; Hort, N.; Kainer, K.U.; Schell, N.; Brokmeier, H.G.; Schreyer, A. Bulk and local textures of pure magnesium processed by rotary swaging. *J. Mag. Alloy.* **2013**, *1*, 341–345. [[CrossRef](#)]
27. Gan, W.M.; Huang, Y.D.; Wang, R.; Wang, G.F.; Srinivasan, A.; Brokmeier, H.G.; Schell, N.; Kainer, K.U.; Hort, N. Microstructures and mechanical properties of pure mg processed by rotary swaging. *Mater. Des.* **2014**, *63*, 83–88. [[CrossRef](#)]
28. Minárik, P.; Zemková, M.; Král, R.; Mhaede, M.; Wagner, L.; Hadzima, B. Effect of microstructure on the corrosion resistance of the AE42 magnesium alloy processed by rotary swaging. *Acta Phys. Pol. A* **2015**, *128*, 805–807. [[CrossRef](#)]
29. Figueiredo, R.B.; Cetlin, P.R.; Langdon, T.G. The processing of difficult-to-work alloys by ecap with an emphasis on magnesium alloys. *Acta Mater.* **2007**, *55*, 4769–4779. [[CrossRef](#)]

30. Vasilev, E.; Linderov, M.; Nugmanov, D.; Sitdikov, O.; Markushev, M.; Vinogradov, A. Fatigue performance of mg-zn-zr alloy processed by hot severe plastic deformation. *Metals* **2015**, *5*, 2316. [[CrossRef](#)]
31. Kirkland, N.T.; Birbilis, N.; Staiger, M.P. Assessing the corrosion of biodegradable magnesium implants: A critical review of current methodologies and their limitations. *Acta Biomater.* **2012**, *8*, 925–936. [[CrossRef](#)] [[PubMed](#)]
32. Delgado, M.C.; García-Galvan, F.R.; Barranco, V.; Feliu Batlle, S. A measuring approach to assess the corrosion rate of magnesium alloys using electrochemical impedance spectroscopy. In *Magnesium Alloys*; IntechOpen: Londone, UK, 2017; pp. 130–159.
33. Nidadavolu, E.P.S.; Feyerabend, F.; Ebel, T.; Willumeit-Römer, R.; Dahms, M. On the determination of magnesium degradation rates under physiological conditions. *Materials* **2016**, *9*, 627. [[CrossRef](#)]
34. Song, G.; Atrens, A. Understanding magnesium corrosion—A framework for improved alloy performance. *Adv. Eng. Mater.* **2003**, *5*, 837–858. [[CrossRef](#)]
35. Kokubo, T.; Takadama, H. How useful is SBF in predicting in vivo bone bioactivity? *Biomaterials* **2006**, *27*, 2907–2915. [[CrossRef](#)] [[PubMed](#)]
36. Xin, Y.; Hu, T.; Chu, P.K. Influence of test solutions on in vitro studies of biomedical magnesium alloys. *J. Electrochem. Soc.* **2010**, *157*, C238–C243. [[CrossRef](#)]
37. Zheng, Y. *Magnesium Alloys as Degradable Biomaterials*; CRC Press: Boca Raton, FL, USA, 2016.
38. Zander, D.; Zumdick, N.A. Influence of Ca and Zn on the microstructure and corrosion of biodegradable Mg–Ca–Zn alloys. *Corros. Sci.* **2015**, *93*, 222–233. [[CrossRef](#)]
39. Bakhsheshi-Rad, H.R.; Hamzah, E.; Fereidouni-Lotfabadi, A.; Daroonparvar, M.; Yajid, M.A.M.; Mezbahul-Islam, M.; Kasiri-Asgarani, M.; Medraj, M. Microstructure and bio-corrosion behavior of Mg–Zn and Mg–Zn–Ca alloys for biomedical applications. *Mater. Corros.* **2014**, *65*, 1178–1187. [[CrossRef](#)]
40. Zhang, B.; Hou, Y.; Wang, X.; Wang, Y.; Geng, L. Mechanical properties, degradation performance and cytotoxicity of Mg–Zn–Ca biomedical alloys with different compositions. *Mater. Sci. Eng. C* **2011**, *31*, 1667–1673. [[CrossRef](#)]
41. Vinogradov, A.; Vasilev, E.; Linderov, M.; Merson, D. Evolution of mechanical twinning during cyclic deformation of Mg–Zn–Ca alloys. *Metals* **2016**, *6*, 304. [[CrossRef](#)]
42. Jardim, P.M.; Solórzano, G.; Sande, J.B.V. Second phase formation in melt-spun Mg–Ca–Zn alloys. *Mater. Sci. Eng. A* **2004**, *381*, 196–205. [[CrossRef](#)]
43. Li, W.-J.; Deng, K.-K.; Zhang, X.; Nie, K.-B.; Xu, F.-J. Effect of ultra-slow extrusion speed on the microstructure and mechanical properties of Mg–4Zn–0.5Ca alloy. *Mater. Sci. Eng. A* **2016**, *677*, 367–375. [[CrossRef](#)]
44. Kubok, K.; Lityńska-Dobrzyńska, L.; Wojewoda-Budka, J.; Góral, A.; Dębski, A. Investigation of structures in as-cast alloys from the Mg–Zn–Ca system. *Arch. Metall. Mater.* **2013**, *58*, 329–333. [[CrossRef](#)]
45. Levi, G.; Avraham, S.; Zilberov, A.; Bamberger, M. Solidification, solution treatment and age hardening of a Mg–1.6 wt.% Ca–3.2 wt.% Zn alloy. *Acta Mater.* **2006**, *54*, 523–530. [[CrossRef](#)]
46. Wasiur-Rahman, S.; Medraj, M. Critical assessment and thermodynamic modeling of the binary Mg–Zn, Ca–Zn and ternary Mg–Ca–Zn systems. *Intermetallics* **2009**, *17*, 847–864. [[CrossRef](#)]
47. Oh, J.C.; Ohkubo, T.; Mukai, T.; Hono, K. TEM and 3DAP characterization of an age-hardened Mg–Ca–Zn alloy. *Scr. Mater.* **2005**, *53*, 675–679. [[CrossRef](#)]
48. Nie, J.F.; Muddle, B.C. Precipitation hardening of Mg–Ca(–Zn) alloys. *Scr. Mater.* **1997**, *37*, 1475–1481. [[CrossRef](#)]
49. Bakhsheshi-Rad, H.R.; Abdul-Kadir, M.R.; Idris, M.H.; Farahany, S. Relationship between the corrosion behavior and the thermal characteristics and microstructure of Mg–0.5Ca–xZn alloys. *Corros. Sci.* **2012**, *64*, 184–197. [[CrossRef](#)]
50. Charni, D.; Ishkina, S.; Epp, J.; Herrmann, M.; Schenck, C.; Zoch, H.W.; Kuhfuss, B. *Generation of Residual Stresses in Rotary Swaging Process*; Dean, T.A., Qin, Y., Vollertsen, F., Yuan, S.J., Eds.; EDP Sciences: Les Ulis, France, 2018.
51. Ma, E. Eight routes to improve the tensile ductility of bulk nanostructured metals and alloys. *JOM* **2006**, *58*, 49–53. [[CrossRef](#)]
52. Niendorf, T.; Canadinc, D.; Maier, H.J.; Karaman, I. The role of grain size and distribution on the cyclic stability of titanium. *Scr. Mater.* **2009**, *60*, 344–347. [[CrossRef](#)]
53. Lapovok, R.; Cottam, R.; Thomson, P.; Estrin, Y. Extraordinary superplastic ductility of magnesium alloy zk60. *J. Mater. Res.* **2005**, *20*, 1375–1378. [[CrossRef](#)]
54. Kim, D.-W.; Suh, B.-C.; Shim, M.-S.; Bae, J.H.; Kim, D.H.; Kim, N.J. Texture evolution in Mg–Zn–Ca alloy sheets. *Met. Mat. Trans. A* **2013**, *44*, 2950–2961. [[CrossRef](#)]

55. Vinogradov, A. Mechanical properties of ultrafine-grained metals: New challenges and perspectives. *Adv. Eng. Mater.* **2015**, *17*, 1710–1722. [[CrossRef](#)]
56. Yasnikov, I.S.; Estrin, Y.; Vinogradov, A. What governs ductility of ultrafine-grained metals? A microstructure based approach to necking instability. *Acta Mater.* **2017**, *141*, 18–28. [[CrossRef](#)]
57. Gu, X.N.; Zhou, W.R.; Zheng, Y.F.; Cheng, Y.; Wei, S.C.; Zhong, S.P.; Xi, T.F.; Chen, L.J. Corrosion fatigue behaviors of two biomedical mg alloys—AZ91d and WE43—In simulated body fluid. *Acta Biomater.* **2010**, *6*, 4605–4613. [[CrossRef](#)] [[PubMed](#)]
58. Bian, D.; Zhou, W.; Liu, Y.; Li, N.; Zheng, Y.; Sun, Z. Fatigue behaviors of Hp-Mg, Mg–Ca and Mg–Zn–Ca biodegradable metals in air and simulated body fluid. *Acta Biomater.* **2016**, *41*, 351–360. [[CrossRef](#)]
59. Nugmanov, D.R.; Sitdikov, O.S.; Markushev, M.V. Texture and anisotropy of yield strength in multistep isothermally forged Mg-5.8Zn-0.65Zr alloy. *IOP Conf. Ser. Mater. Sci. Eng.* **2015**, *82*, 012099. [[CrossRef](#)]
60. Markushev, M.V.; Nugmanov, D.R.; Sitdikov, O.; Vinogradov, A. Structure, texture and strength of Mg-5.8Zn-0.65Zr alloy after hot-to-warm multi-step isothermal forging and isothermal rolling to large strains. *Mater. Sci. Eng. A* **2018**, *709*, 330–338. [[CrossRef](#)]
61. Ogarevic, V.V.; Stephens, R.I. Fatigue of magnesium alloys. *Ann. Rev. Mater. Sci.* **1990**, *20*, 141–177. [[CrossRef](#)]
62. Di Mario, C.; Griffiths, H.; Goktekin, O.; Peeters, N.; Verbist, J.; Bosiers, M.; Deloose, K.; Heublein, B.; Rohde, R.; Kasese, V.; et al. Drug-eluting bioabsorbable magnesium stent. *J. Interv. Cardiol.* **2004**, *17*, 391–395. [[CrossRef](#)] [[PubMed](#)]
63. Erne, P.; Schier, M.; Resink, T.J. The road to bioabsorbable stents: Reaching clinical reality? *Cardiovasc. Interv. Radiol.* **2006**, *29*, 11–16. [[CrossRef](#)]
64. Komai, K. 4.13—Corrosion fatigue. In *Comprehensive Structural Integrity*; Milne, I., Ritchie, R.O., Karihaloo, B., Eds.; Pergamon: Oxford, UK, 2003; pp. 345–358.
65. Hilpert, M.; Wagner, L. Corrosion fatigue behavior of the high-strength magnesium alloy AZ80. *J. Mater. Eng. Perform.* **2000**, *9*, 402–407. [[CrossRef](#)]
66. Eliezer, A.; Gutman, E.M.; Abramov, E.; Unigovski, Y. Corrosion fatigue of die-cast and extruded magnesium alloys. *J. Light Met.* **2001**, *1*, 179–186. [[CrossRef](#)]
67. Singh Raman, R.K.; Jafari, S.; Harandi, S.E. Corrosion fatigue fracture of magnesium alloys in bioimplant applications: A review. *Eng. Fract. Mech.* **2015**, *137*, 97–108. [[CrossRef](#)]
68. Tunold, R.; Holtan, H.; Berge, M.-B.H.; Lasson, A.; Steen-Hansen, R. The corrosion of magnesium in aqueous solution containing chloride ions. *Corros. Sci.* **1977**, *17*, 353–365. [[CrossRef](#)]
69. Atrens, A.; Song, G.-L.; Liu, M.; Shi, Z.; Cao, F.; Dargusch, M.S. Review of recent developments in the field of magnesium corrosion. *Adv. Eng. Mater.* **2015**, *17*, 400–453. [[CrossRef](#)]
70. Ullmann, B.; Reifenrath, J.; Seitz, J.-M.; Bormann, D.; Meyer-Lindenberg, A. Influence of the grain size on the in vivo degradation behaviour of the magnesium alloy LAE442. *Proc. Inst. Mech. Eng. Part H: J. Eng. Med.* **2013**, *227*, 317–326. [[CrossRef](#)] [[PubMed](#)]
71. Gehrman, R.; Frommert, M.M.; Gottstein, G. Texture effects on plastic deformation of magnesium. *Mater. Sci. Eng. A* **2005**, *395*, 338–349. [[CrossRef](#)]
72. Biswas, S.; Singh Dhinwal, S.; Suwas, S. Room-temperature equal channel angular extrusion of pure magnesium. *Acta Mater.* **2010**, *58*, 3247–3261. [[CrossRef](#)]
73. Agnew, S.R.; Horton, J.A.; Lillo, T.M.; Brown, D.W. Enhanced ductility in strongly textured magnesium produced by equal channel angular processing. *Scr. Mater.* **2004**, *50*, 377–381. [[CrossRef](#)]
74. Beausir, B.; Suwas, S.; Tóth, L.S.; Neale, K.W.; Funderberger, J.-J. Analysis of texture evolution in magnesium during equal channel angular extrusion. *Acta Mater.* **2008**, *56*, 200–214. [[CrossRef](#)]
75. Gzyl, M.; Rosochowski, A.; Boczkal, S.; Olejnik, L. The role of microstructure and texture in controlling mechanical properties of AZ31b magnesium alloy processed by i-ecap. *Mater. Sci. Eng. A* **2015**, *638*, 20–29. [[CrossRef](#)]
76. Agnew, S.R.; Yoo, M.H.; Tome, C.N. Application of texture simulation to understanding mechanical behavior of mg and solid solution alloys containing Li or Y. *Acta Mater.* **2001**, *49*, 4277–4289. [[CrossRef](#)]
77. Kleiner, S.; Uggowitzer, P.J. Mechanical anisotropy of extruded Mg–6% Al–1% Zn alloy. *Mater. Sci. Eng. A* **2004**, *379*, 258–263. [[CrossRef](#)]
78. Liang, S.J.; Liu, Z.Y.; Wang, E.D. Microstructure and mechanical properties of Mg–Al–Zn alloy deformed by cold extrusion. *Mater. Lett.* **2008**, *62*, 3051–3054. [[CrossRef](#)]

79. Gottstein, G.; Al Samman, T. Texture development in pure mg and mg alloy AZ31. *Mater. Sci. Forum* **2005**, *495*, 623–632. [[CrossRef](#)]
80. Al-Samman, T.; Li, X. Sheet texture modification in magnesium-based alloys by selective rare earth alloying. *Mater. Sci. Eng. A* **2011**, *528*, 3809–3822. [[CrossRef](#)]
81. Zhang, B.; Wang, Y.; Geng, L.; Lu, C. Effects of calcium on texture and mechanical properties of hot-extruded Mg–Zn–Ca alloys. *Mater. Sci. Eng. A* **2012**, *539*, 56–60. [[CrossRef](#)]
82. Masood Chaudry, U.; Hoo Kim, T.; Duck Park, S.; Sik Kim, Y.; Hamad, K.; Kim, J.-G. On the high formability of AZ31-0.5Ca magnesium alloy. *Materials* **2018**, *11*, 2201. [[CrossRef](#)] [[PubMed](#)]
83. Kim, S.-H.; You, B.-S.; Dong Yim, C.; Seo, Y.-M. Texture and microstructure changes in asymmetrically hot rolled AZ31 magnesium alloy sheets. *Mater. Lett.* **2005**, *59*, 3876–3880. [[CrossRef](#)]
84. Estrin, Y.; Yi, S.B.; Brokmeier, H.G.; Zuberova, Z.; Yoon, S.C.; Kim, H.S.; Hellmig, R.J. Microstructure, texture and mechanical properties of the magnesium alloy AZ31 processed by ecap. *Int. J. Mater. Res.* **2008**, *99*, 50–55. [[CrossRef](#)]
85. Serebryany, V.N.; Ivanova, T.M.; Savyolova, T.I.; Dobatkin, S.V. Effect of texture on tensile properties of an ecap-processed MA2-1 magnesium alloy. *Solid State Phenom.* **2010**, *160*, 159–164. [[CrossRef](#)]
86. Tong, L.B.; Zheng, M.Y.; Hu, X.S.; Wu, K.; Xu, S.W.; Kamado, S.; Kojima, Y. Influence of ecap routes on microstructure and mechanical properties of Mg–Zn–Ca alloy. *Mater. Sci. Eng. A* **2010**, *527*, 4250–4256. [[CrossRef](#)]
87. Agnew, S.R.; Mehrotra, P.; Lillo, T.M.; Stoica, G.M.; Liaw, P.K. Texture evolution of five wrought magnesium alloys during route a equal channel angular extrusion: Experiments and simulations. *Acta Mater.* **2005**, *53*, 3135–3146. [[CrossRef](#)]
88. Agnew, S.R.; Mehrotra, P.; Lillo, T.M.; Stoica, G.M.; Liaw, P.K. Crystallographic texture evolution of three wrought magnesium alloys during equal channel angular extrusion. *Mater. Sci. Eng. A* **2005**, *408*, 72–78. [[CrossRef](#)]
89. Kabirian, F.; Khan, A.S.; Gnäupel-Herlod, T. Plastic deformation behavior of a thermo-mechanically processed AZ31 magnesium alloy under a wide range of temperature and strain rate. *J. Alloy. Compd.* **2016**, *673*, 327–335. [[CrossRef](#)]
90. Segal, V.M. Severe plastic deformation: Simple shear versus pure shear. *Mater. Sci. Eng. A* **2002**, *338*, 331–344. [[CrossRef](#)]



© 2019 by the authors. Licensee MDPI, Basel, Switzerland. This article is an open access article distributed under the terms and conditions of the Creative Commons Attribution (CC BY) license (<http://creativecommons.org/licenses/by/4.0/>).